

Three-Dimensional Fourier Scattering Transform and Classification of Hyperspectral Images

Ilya Kavalero, Weilin Li, Wojciech Czaja, and Rama Chellappa, *Fellow, IEEE*

Abstract—Recent research has resulted in many new techniques that are able to capture the special properties of hyperspectral data for hyperspectral image analysis, with hyperspectral image classification as one of the most active tasks. Time-frequency methods decompose spectra into multi-spectral bands, while hierarchical methods like neural networks incorporate spatial information across scales and model multiple levels of dependencies between spectral features. The Fourier scattering transform is an amalgamation of time-frequency representations with neural network architectures, both of which have recently been proven to provide significant advances in spectral-spatial classification. We test the proposed three dimensional Fourier scattering method on four standard hyperspectral datasets, and present results that indicate that the Fourier scattering transform is highly effective at representing spectral data when compared with other state-of-the-art spectral-spatial classification methods.

Index Terms—Scattering transform, Fourier scattering transform, hyperspectral image (HSI), supervised classification, convolutional neural networks

I. INTRODUCTION

Hyperspectral image sensors routinely collect hundreds of bands of different wavelength channels of the surface of the Earth [1]. Due to the rapidly growing amount of available hyperspectral image (HSI) data [2], there is much interest in the development of algorithms that automatically classify the pixels of a hyperspectral image. However several characteristics of HSI data make this task challenging: the high-dimensionality of the data, the low spatial resolution which results in unfavorable signal-to-noise ratio, and that labeled data is scarce and typically not transferable across different datasets due to e.g., location and weather effects.

As the review by He *et al.* [3] noted, neural networks (NNs) and deep learning, having achieved breakthroughs in image classification, is starting to be applied to hyperspectral image processing [4], [5], [6], [7], [8], to some advantages and

disadvantages. The hierarchical network for feature extraction at multiple levels has a potential to produce highly informative features for classification, but there is a great number of parameters to train which results in long training times. At the same time, time-frequency analysis for HSI has recently proven to provide both meaningful and high quality results [9], [3], [10], especially when the filters are specifically designed for HSI data [11]. These time-frequency tools are an underutilized tool when compared with the more popular wavelet based methods [12], [13], [14], [15], [16], [17].

The *Fourier scattering transform* (FST), introduced in [18], [19], can be viewed as a modern time-frequency approach to machine learning. It unifies deep learning architectures with time-frequency generated filters in order to capture higher order correlations between time-frequency representations. The FST uses fixed filters instead of adaptable or learned ones such as those in NNs, but the FST does not require computationally expensive training and enjoys theoretical guarantees that NNs lack. In particular, the FST automatically removes small diffeomorphic nonlinearities or perturbations such as noise, which are typically irrelevant in classification tasks. The *three-dimensional Fourier scattering transform* (3D FST) is a special case of the FST which is obtained by employing three dimensional time-frequency generated filters. When used on HSI data, it provides a multi-layer spatial-spectral decomposition. We argue that the spectra generated by standard material classes are more discriminable in the time-frequency domain compared to other representations. This argument was also made in [11], which showed that decomposing the signal using time-frequency filters provides informative features for HSI data. However, the 3D FST further refines this idea by integrating together the spectral and spatial information, and incorporating them into a multi-layer setting, where deeper layers capture more complex features.

We demonstrate that the 3D FST provides state-of-the-art performance on HSI data. We compare to results with various neural network, wavelet, and scattering based methods [12], [5], [20], [11], [21], [8], [7], [16], [15], [17], [22], [23], [17]. One notable method that we carefully compare with is the *three-dimensional wavelet scattering transform* (3D WST). The *wavelet scattering transform* (WST) was originally developed by Mallat [24] and the 3D WST was applied to HSI classification in [17]. Our results show that time-frequency Fourier features are more suitable than time-scale wavelet features for HSI discrimination and classification purposes. We obtain state of the art results on the Indian Pines, Pavia University, and Pavia Center datasets at 10%, 10%, and 1% of training data respectively. We also provide an open

Manuscript Submitted June 16, 2019. This work was supported in part by the MURI from the Army Research Office under the Grant No. W911NF-17-1-0304. This is part of the collaboration between US DOD, UK MOD and UK Engineering and Physical Research Council (EPSRC) under the Multidisciplinary University Research Initiative. This work was also supported in part by LTS through Maryland Procurement Office and the NSF DMS 1738003 grant. (*Corresponding author: Ilya Kavalero*)

I. Kavalero and R. Chellappa are with UMIACS, University of Maryland at College Park, College Park, MD 20742 USA (e-mail: ilyak@umiacs.umd.edu; rama@umiacs.umd.edu)

W. Li was with the Norbert Wiener Center, University of Maryland at College Park, College Park, MD 20742 USA. He is now with the Courant Institute of Mathematical Sciences, New York University, NY 10012 USA (e-mail: weilinli@cims.nyu.edu)

W. Czaja is with the Norbert Wiener Center, University of Maryland at College Park, College Park, MD 20742 USA (e-mail: wojtek@math.umd.edu)

source implementation of all code used for our algorithms and experiments.¹

The rest of this paper is organized as follows. Section II-A reviews related work on using neural networks, wavelets, and time-frequency bases for feature extraction and the classification of HSI data. Section II-B provides background information on scattering transforms. Section III defines the 3D FST and how it provides a joint spectral-spatial representation suited for HSI data. Section IV introduces the datasets that 3D FST is evaluated on, explains the parameter choices in the 3D FST, and discusses the results on these datasets while comparing them to other competing methods. Section V concludes the paper.

II. RELATED WORK

A. Previous Work

Many methods in the literature have concentrated solely on the spectrum for the classification of HSI data. More recently, to improve classification performance spectral-spatial techniques which better exploit the properties of HSI data have become popular. Our review of neural network, wavelet, and time-frequency based methods can be roughly split into four categories: 1) purely spectral techniques 2) spectral methods that incorporate spatial pre/post processing, 3) purely spatial methods that may include spectral pre/post processing, and 4) those that integrate spectral-spatial information at once.

- 1) Pixelwise methods that extract wavelet, time-frequency, and neural network features solely in the spectral domain have been developed to address these challenges in HSI classification [25], [21], [26], [20], [27], [23]. The neural network (NN) family of methods iteratively composes layers of matrix multiplications or linear convolutions with a pointwise non-linear function. The weights in these matrices or convolution filters are adapted using backpropagation during an initial training phase. NNs consisting of 1D convolutions with spectra [21], and 2D convolutions of reshaped 1D spectra vectors [26], as well as other Deep Belief Networks (DBN) [23] have been evaluated. Another family of methods are the wavelet and time-frequency methods which use a pre-determined basis to extract edge like features. 1D Morlet wavelet features with trainable scale and translation parameters have been extracted and input to a 2 layer NN [25], [28]. A compromise between the learned and potentially deep and complex neural networks and classical wavelet features are scattering transforms, which are particular types of operators introduced by Mallat [24] whose coefficients are computed with a hierarchical network structure that captures invariances in data. 1D Fourier scattering features coupled with an SVM have also proved to be effective, outperforming 1D wavelet scattering features [27]. These purely spectral methods improve upon the performance of simpler machine learning algorithms, like the application of SVMs on the 1D spectra of each pixel, but ignore the significant spatial structure present in HSI data.

- 2) A variety of methods have successfully used spatial information in pre-processing steps (more rarely post-processing as well) to improve classification performance while still focusing on the spectral aspects of the data [7], [29], [4], [30], [31]. Ashitha *et al.* [31] classify 1D wavelet scattering features with an SVM after smoothing each channel of the HSI with 2D Gaussian filters. Sandwiching a spectral NN between two 2D Gaussian blur layers with trainable variance greatly improves performance and remains one of the most competitive HSI methods [7]. Lee *et al.* followed up on this work a deep spectral NN with residual connections following a single 3D filter layer [29]. Acquarelli *et al.* made changes instead to the training process and included a spatial term in the regularizer of a purely spectral 1D convolutional neural network (CNN) [4].
- 3) Spatial methods that include some spectral pre-processing have also been applied to HSI data [22], [8], [5], [13], [27], [6]. Classical 2D CNNs and Recurrent CNNs (RCNN) have been used on each channel of HSI input independently [22]. Also popular has been using PCA or other dimensionality reduction methods to reduce the number of channels in the the HSI before using a 2D CNN [8], [5], or 2D wavelet scattering [13]. Our previous work performed competitively using 1D Fourier scattering preprocessing followed by 2D wavelet scattering [27]. Recently Deng *et al.* used a new CapsNet NN architecture [32] with 2D filters on each channel independently to achieve competitive results.
- 4) Integrated spectral-spatial methods combine information from spectral signatures and spatial neighborhoods simultaneously, and are also common. Some methods consider sequences of 1D spectra [20] (for example in variety of NN called Long Short Term Memory or LSTM) or flatten the HSI cube to a matrix and use 2D methods [33], but by far the most popular methods involve building 3D filters [22], [5], [15], [10], [14], [11], [16], [12], [17], [9]. 3D convolutional layers in NNs, CNNs, and RCNNs, both shallow and deep have been evaluated [5], [22]. But the lack of training data challenges models with many learnable parameters, and these networks struggled in comparison to methods with predetermined filters such as the 3D Gabor wavelets that Shen and Jia *et al.* used to extract features [15], [10], [14], and classify with a variety of algorithms, for instance a sparse representation based classification (3D WT+SRC) [15]. Bau *et al.* [9] used the real part of 3D Gabor filters sampled densely in the time-frequency domain to get features used with a Mahalanobis distance classifier. He *et al.* [11] decomposed the same filter into 8 subfilters, using only 3 to construct a discriminative low-rank Gabor mother filter (DLRGF) used to extract features, a hand designed feature which proved to be very competitive with a least squares based classifier (3D DLRGF+LS). Qian and Cao *et al.* [16], [12] used a Haar 3D wavelet filter bank (3D DWT-FB) and discrete wavelet transform (3D DWT) with various classifiers. Tang *et al.* [17] proposed a 3D Gabor wavelet scat-

¹<https://github.com/ilyakava/tfST>

tering approach to extract features (3D WST), which decomposes the HSI across multiple wavelet scales and orientations and uses local averaging to keep class labels consistent in neighborhoods, and classified with a radial basis function SVM (3D WST+RBF-SVM).

The paradigm that we have ordered our review by has been the degree to which each method integrates spectral-spatial information, which greatly affects classification performance. Another characteristic to distinguish HSI methods worth mentioning is the amount of dependency or interaction between the spectral-spatial features that each technique models, as [3] points out.

In the terminology of [3], the simplest *dependency system* is the case where features are extracted directly from the HSI data. This encompasses the majority of the methods we presented. However neural networks with multiple layers naturally model a hierarchical interaction of features, with as many degrees of interaction as number of layers in the network: [6], [20], [5], [4], [26], [23], [29], [22], [8], [21]. The same can be said for the layers of scattering networks: [17], [33], [13], [31], [27]. This distinguishes these two classes of approaches from purely wavelet [34], [12], [15], [16] or time-frequency methods [11], [9], [3], [10], and yields more sophisticated features that yield better classification results, as we show in Section IV.

B. Fourier Scattering Transform

We begin by formally defining the scattering transform. Fix a sequence $\Phi = \{\phi, \phi_\lambda\}_{\lambda \in \Lambda}$ of square integrable functions on \mathbb{R}^d , where Λ is the index set of the sequence. Given an input function f defined on \mathbb{R}^d , we iteratively convolve it with this sequence and take the modulus in the following way. For each index $\lambda \in \Lambda$, let

$$U[\lambda](f) = |f * \phi_\lambda|,$$

where $*$ is the convolution of functions on \mathbb{R}^d . We can extend this rule to multi-indices. For each $\lambda = (\lambda_1, \dots, \lambda_k) \in \Lambda^k$, let

$$U[\lambda](f) = U[\lambda_k] \cdots U[\lambda_1](f).$$

The *scattering transform* \mathcal{S}_Φ associated with Φ is formally defined as the sequence of functions

$$\mathcal{S}_\Phi(f) = \{f * \phi, U[\lambda](f) * \phi\}_{\lambda \in \Lambda^k, k \geq 1}.$$

See Figure 1 for a visualization of the scattering transform as a convolutional neural network.

The mathematical properties of the scattering transform and the features that it generates greatly depend on the underlying sequence of functions. Mallat [24] and his collaborators [35] primarily considered the wavelet (time-scale) case, where ϕ is the father wavelet and $\{\phi_\lambda\}_{\lambda \in \Lambda}$ are dilations of the mother wavelet function. The resulting transform is called the *wavelet scattering transform* (WST) and it provides a powerful multi-scale representation [35]. In contrast, two authors of this paper studied the time-frequency analogue [18], [19], where ϕ is a band-limited function and $\{\phi_\lambda\}$ are modulations of ϕ . The resulting transformation is called the *Fourier scattering*

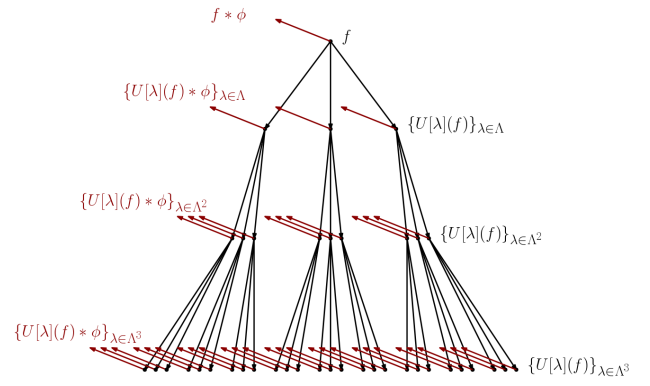


Fig. 1. The network structure of the scattering transform. The functions $U[\lambda](f)$ can be computed iteratively and they are represented by the black dots. The scattering coefficients of f , represented by the red dots, are found by convolving the each $U[\lambda](f)$ with ϕ .

transform (FST) and it provides a hierarchical time-frequency representation of the data.

Although wavelet based techniques have recently dominated the field of HSI analysis due to their overall impact on image processing, see e.g., [25], [15], [10], [12], time-frequency methods form a natural foundation for spectral data exploration. They were the basis for the early Fourier transform imaging spectroscopy methods [36], [37], as well as for recent attempts to analyze hyperspectral imagery [11].

The wavelet and Fourier scattering transforms provide entirely different representations: the WST computes localization and scale characteristics, whereas the FST provides frequency distribution information. Nonetheless, and perhaps surprisingly, both transformations satisfy similar properties: they are energy preserving, are non-expansive, and contract sufficiently small translations and diffeomorphisms, see the theorems in [24], [18] for precise estimates. These properties explain why they are effective feature extractors, since small perturbations typically have no effect on a data point's label. In the context of hyper-spectral image classification, the spectra of similar components have common characteristics up to small deviations, which are then removed by either the FST or WST.

A scattering transform has an infinite number of layers and each node has infinitely many children. Thus, we can only compute a finite subset of the coefficients, but not all scattering transforms can be truncated in a faithful way. Thankfully, the FST can be truncated without destroying its properties. Indeed, theoretical results guarantee that the total energy contained in the k -th order FST coefficients is at most ε^{k-1} of the original energy of f for some small $\varepsilon \in (0, 1)$, see [18].

III. METHODOLOGY

The FST is a generic transformation that is suitable for many applications and purposes. To differentiate between the generic FST with the particular kind that we use in this paper for hyperspectral image classification, we shall call the latter as the *three-dimensional Fourier scattering transform* (3D FST), which we describe below.

In the context of HSI data, we have $d = 3$ and we view a HSI as a function f defined on a rectangular subset of \mathbb{Z}^3 . That

is, $f(x, y, b)$ is the value of the image at spatial location (x, y) and band b . Fix a function g on \mathbb{Z}^d , which is typically called the *window function*. Following standard convention, we select the window g to be compactly supported in a 3-dimensional rectangle with side lengths $M = (M_1, M_2, M_3)$. Let Λ_M be the collection of $m \in \mathbb{Z}^3$ such that $0 \leq m_j \leq M_j - 1$ for each j . We define the functions $\{g_m\}_{m \in \Lambda_M}$ by the formula,

$$g_m(x, y, b) = \exp\left(2\pi i\left(\frac{xm_1}{M_1} + \frac{ym_2}{M_2} + \frac{bm_3}{M_3}\right)\right)g(x, y, b). \quad (1)$$

Here, x and y are the spatial coordinates and b is the spectral coordinate.

There is the usual trade-off with time-frequency representations: Larger values of M provide worse spatial localization but better frequency resolution, whereas a smaller M yields the opposite effect. For this reason, it is reasonable to use different functions in each layer of the network to maximize the performance of the transform. Let $M' = (M'_1, M'_2, M'_3)$ and $M'' = (M''_1, M''_2, M''_3)$ be multi-integers and let g' and g'' denote functions supported in rectangles of size M' and M'' respectively. We define $\{g'_m\}_{m \in \Lambda_{M'}}$ and $\{g''_m\}_{m \in \Lambda_{M''}}$ analogous to the definition of g_m given in equation (1), except with M' and M'' replacing M and g' and g'' replacing g , respectively.

Time-frequency representations are inherently redundant. We can down-sample the features in such a way that we do not lose important information, e.g. see [38], and this type of result is closely related to the classical Shannon sampling theorem. In our case, we only down-sample in the spectral dimension. We fix a positive integers P, P', P'' which shall be the downsampling factors in the each of the three layers.

The zero order 3D FST coefficient $S_0(f)$, is defined as

$$S_0(f)(x, y, b) = (f * g)(x, y, Pb).$$

Here, $*$ denotes the convolution operator on \mathbb{Z}^3 . This is simply a local averaging of the input by the window function g and down-sampled by P . The first order intermediate 3D FST coefficients are

$$U_m(f)(x, y, b) = |(f * g_m)(x, y, Pb)|.$$

The collection $\{U_m(f)\}_{m \in \Lambda_M}$ can be interpreted as the modulus of the *windowed Fourier transform* of f (also called the *short-time Fourier transform* in signal processing or the *spectrogram* in audio processing).

The windowed Fourier transform is not stable to small perturbations of the input function. The basic reason is that if f consists of a single high frequency component, then there exists a \tilde{f} such that \tilde{f} is a small diffeomorphism of f and its frequency support is disjoint from that of f ; consequently, f and \tilde{f} are very different in both the L^2 metric, see [24], [39] for a rigorous analysis. To avoid for this behavior, the scattering transform proposes to locally average $U_m(f)$ with g' . The first order 3D FST coefficients are

$$S_m(f)(x, y, b) = (U_m(f) * g')(x, y, P'b).$$

Hence, the first order 3D FST coefficients carry information about a spatially-averaged short-time Fourier transform of f .

While naive local averaging improves stability to small deformations, it also removes a significant amount of high-frequency information because g is a low-pass function. The lost components are included in the functions, $U_m(f) * g_n$. However, these functions suffer from the same instability properties as $U_m(f)$. The second order intermediate 3D FST coefficients are

$$U_{m,n}(f)(x, y, b) = |(U_m(f) * g'_n)(x, y, P'b)|.$$

These intermediate coefficients are also unstable to small diffeomorphisms, so we perform a local averaging. The second order 3D FST coefficients are

$$S_{m,n}(f)(x, y, b) = (U_{m,n}(f) * g'')(x, y, P''b).$$

We also note that theoretical results in [18] guarantee that $S_{m,n}(f)$ is small when $n \geq m$, so we can improve the computational efficiency of the algorithm by only computing the coefficients for which $n \neq m$.

The zero and first order 3D FST coefficients can be interpreted as spatially-smoothed versions of classical spectral-spatial representations. It is not as obvious what the second order coefficients represent. At first glance, the second order 3D FST coefficients appear similar to the Mel-frequency cepstral coefficients (MFCCs), but there is an important distinction. The MFCCs are calculated by fixing the spatial coordinate and then further decomposing the spectrogram along the frequency axis in log scale. MFCCs play an important role in audio analysis because more global characteristics, which are not captured by the spectrogram, contain important information.

In contrast to the MFCCs, the second order 3D FST coefficients are calculated by fixing the spectral variable and then further decomposing along the spatial coordinate. That is, $U_{m,n}(f)$ describes whether the m -th frequency of f over intervals of length M (a local property captured by the first order coefficients) varies at frequency n over intervals of length MM' (a more global property).

In summary, given a hyperspectral image f , the features generated by the 3D FST at location (x, y) are the collection of vectors

$$\begin{aligned} \text{Zero order: } & S_0(f)(x, y, \cdot) \\ \text{First order: } & \{S_m(f)(x, y, \cdot)\}_{m \in \Lambda_M} \\ \text{Second order: } & \{S_{m,n}(f)(x, y, \cdot)\}_{m \in \Lambda_M, n \in \Lambda_{M'}} \end{aligned}$$

These vectors are concatenated to form a feature vector for each pixel (x, y) of the hyperspectral image f .

IV. EXPERIMENTS AND RESULTS

A. Data Sets

We test the performance of these feature extractors on the following hyper-spectral databases:

- *Indian Pines (IP)* acquired over the Indian Pines test site in Northwestern Indiana in 1992 by the Airborne Visible / Infrared Imaging Spectrometer (AVIRIS) sensor [40].
- *Pavia University (PaviaU)* acquired during a 2001 flight campaign over Pavia, northern Italy, using the reflective optics system imaging spectrometer (ROSIS) sensor [41].

- *Botswana* acquired over the Okavango Delta, Botswana in 2001, by the Hyperion sensor on the NASA EO-1 satellite [42].
- *Pavia Center (PaviaC-R)* acquired in 2001 over Pavia, northern Italy, using the ROSIS sensor [43]. We use only the right half of the Pavia Center dataset as it contains the majority of the labeled pixels.
- *Smith Island* captured by a Airborne Hyperspectral Scanner (HyMAP) on in 2000 over Smith Island, VA, a barrier island in the Virginia Coast Reserve. [44]

Table I shows additional information on all five datasets. The ground truth and labels for the five datasets are in Figs. 2 to 6. Datasets 1-5 can be downloaded from the webpage [45].

B. Experimental Setup

When using the Fourier scattering transform on HSI data, there are several parameter choices that impact the effectiveness of the method. Recall that g, g', g'' are the window functions used in each layer of the 3D FST, where M, M', M'' are the size of their supports, and P, P', P'' are the down-sampling parameters. For simplicity, in most of our experiments, we set $M = M' = M'', P = P' = P'',$ and $g = g' = g''$ is the rectangular window.

Each dataset has a different number of pixels, spectral dimension, and ratio of labeled to unlabeled pixels as seen in Table I, so we vary parameters of the feature extractors for each dataset. After extensive testing with 10% of training data, here are the parameters that tend to provide the best results:

- *Indian Pines.* We set $M = (11, 11, 5)$ and $M' = M'' = (11, 11, 3)$ and downsample by 3 in the spectral dimension.
- *PaviaU and PaviaC-R.* We set $M = M' = M'' = (7, 7, 7)$ and downsample by 3 in the spectral dimension.
- *Botswana.* For the first layer we set $M = (11, 11, 3)$ and we do not downsample. Otherwise we set $M' = M'' = (11, 11, 8)$ and we downsample by 8 in the spectral dimension.
- *Smith Island.* We set $M = M' = M'' = (9, 9, 5)$ and downsample by 3 in the spectral dimension.

To make a fair and consistent comparison, we use the same linear *support vector machine* (SVM) as the classifier for each feature extractor and dataset. We train a SVM on a fraction of the labeled data and use the remainder for testing purposes. SVM aims to optimally separate the labeled data points into two disjoint classes and then classify the remaining ones according to this boundary. The SVM is implemented in Scikit-learn with default parameters.

We also evaluate using filters determined by the 3D WST by Tang *et al.* [17]. We implement the same feature extraction method and use the parameters recommended by Tang *et al.* There, the optimal parameters for 3D WST were determined to be filters of size $7 \times 7 \times 7$ for two layers, with 9 orientations and 3 scales per layer. Their work also uses scale increasing paths analogous to frequency decreasing paths.

C. Analysis of Computational Cost

In Table II is the runtime performance of 3D FST and 3D WST. In our implementation we classified one pixel at

a time, so the feature extraction performance is simply the number of pixels our scattering network could process at one time. In the classification setting, after all the labelled pixels were processed, a linear SVM was trained, and then the test samples were classified. The SVM performance numbers in Table II are computed from the test SVM, and the training was always faster than the testing of the SVM. The major factor in performance was not the filter size directly, but the number of filters used in total. In our experiments the number of filters per layer was the product of the size of the supports of the filters in each dimension, for example in the first layer the number of filters was $M_1 \times M_2 \times M_3$. For example after the first layer, our Botswana Fourier scattering network had 3 times as many filters as our Pavia network, and we see that it took 3 times as long to compute the features per pixel. Since the SVM did not take much time total, we saw no need to run PCA or any other form of dimension reduction between feature extraction and classification, though it could have reduced memory usage by throwing away some coefficients. All our networks were designed so that the features for all the labelled pixels of each dataset could fit on a NVidia Titan X GPU with 12 GB of memory.

D. Discussion of Results

The accuracy tables for the feature extractors and datasets are displayed in Tables III to VII. The numbers were obtained by averaging 10 trials and the numbers in parentheses indicate the standard deviation of the results for these trials. We choose approximately 10%, 10%, 5%, 1%, and 5% of the labeled pixels, uniformly at random, in Indian Pines, Pavia University, Botswana, Pavia Center, and Smith Island, respectively, as training data for the linear SVM. Since we compare our method to the 3D WST method introduced in [17], we use their same dataset for PaviaU and Botswana, and for Indian Pines we use a dataset from [7] which has a slightly fewer number of training samples for every class. 3D WST with a linear SVM performs within a margin of error with 3D WST with a RBF-SVM, as reported by Tang *et al.* [17]: 95.98 (± 0.46) vs 94.46 (± 0.79) OA on Indian Pines at 10%, 99.22 (± 0.10) vs 99.30 (± 0.12) OA on PaviaU at 10%, and 96.98 (± 1.06) vs 97.57 (± 1.25) OA on Botswana at 5% for 3D WST vs 3D WST+RBF-SVM. We use a less powerful linear SVM with no hyperparameters tuned throughout when we report and spend no time on classifier specific model validation, for brevity we abbreviate with 3D FST and 3D WST instead of 3D FST+SVM and 3D WST+SVM. The classification maps for 3D FST and 3D WST are in Figs. 2 to 6. A comparison of our methods to the results in the literature for Indian Pines and PaviaU are in Tables VIII and IX.

The relatively uniform and dense geometric distribution of the ground truth for Indian Pines, PaviaU, and PaviaC, makes it is easy to see the tradeoffs between time-scale and time-frequency scattering when looking at the classification maps, in addition to the per class accuracies. On these three datasets, the only disagreements appear on the edges of class shapes. In particular, on PaviaU 3D FST improves upon the accuracy of every class. It smooths and corrects sensible mistakes that

Name	Satellite	No. Bands	Bandwidth	Meters per Pixel	Dimensions HxW	No. Labeled Pixels	No. Classes
PaviaU	ROSIS	103	430-860 nm	1.3 m	610x340	42776	9
PaviaC-R	ROSIS	102	430-860 nm	1.3 m	1096x492	103539	9
IP	AVIRIS	200	400-2500 nm	3.7 m	145x145	10249	16
Smith Island	HyMAP	117	445-2486 nm	4.5 m	679x944	2743	22
Botswana	NASA EO-1	145	400-2500 nm	30 m	1476x256	3248	14

TABLE I
ATTRIBUTES OF THE DATASETS USED.

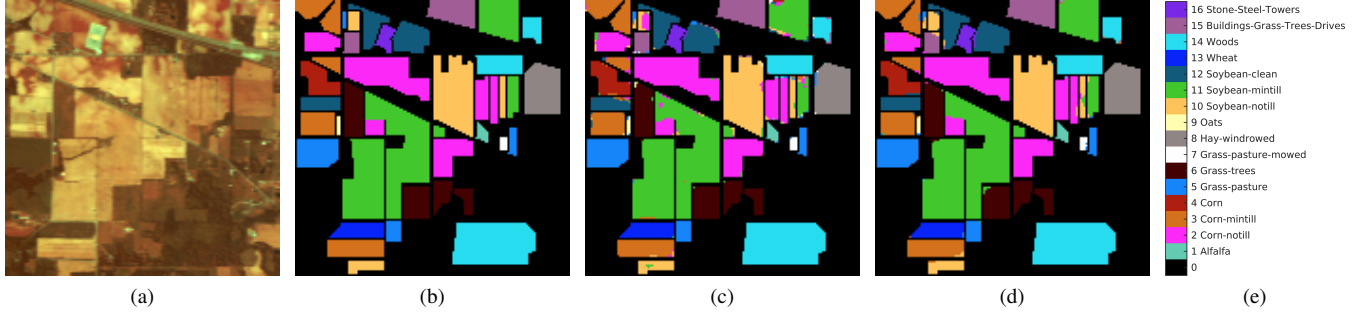


Fig. 2. Indian Pines (a) False color image and (b) Ground Truth Labels. Classification results for (c) 3D WST and (d) 3D FST. (e) Class Labels.

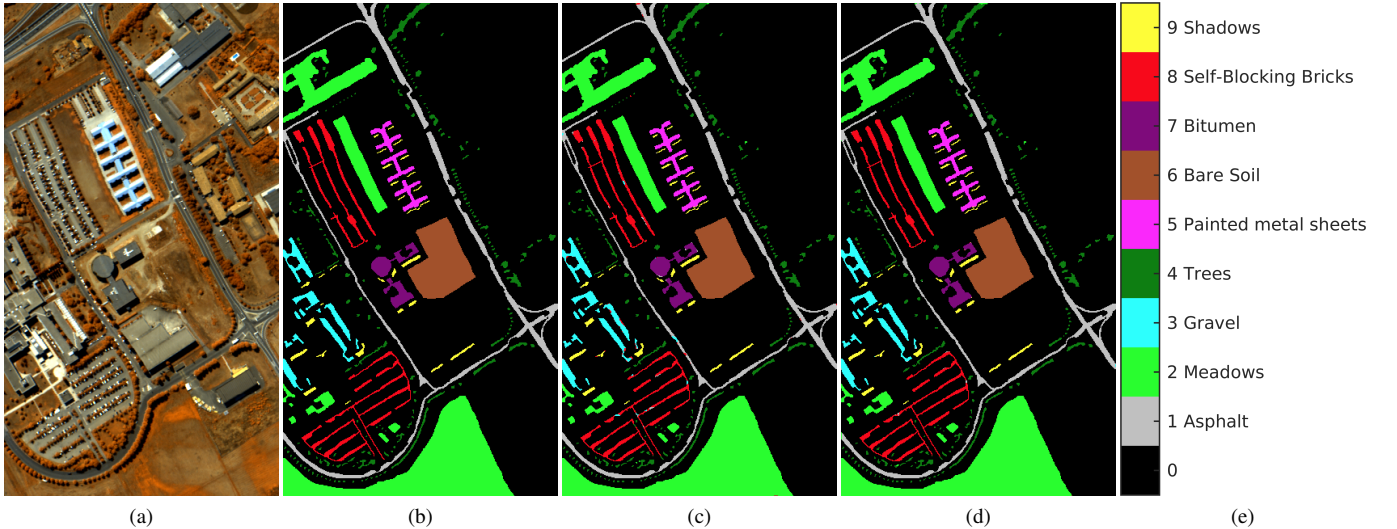


Fig. 3. Pavia University (a) False color image and (b) Ground Truth Labels. Classification results for (c) 3D WST and (d) 3D FST. (e) Class Labels.

TABLE II
FEATURE EXTRACTION AND SVM PERFORMANCE IN PIXELS / SECOND.

	IP	PaviaU	PaviaC	Botswana	Smith
3D WST Feat.	119.4	207.7	203.7	155.6	177.2
3D FST Feat.	30.5	19.9	20.5	7.6	16.9
SVM for 3D WST	42.6	138.6	492.8	384.7	373.7
SVM for 3D FST	84.5	67.7	334.9	205.2	290.6

3D WST makes along the edges: confusing gravel and bricks, and asphalt for both. For PaviaC, 3D FST and 3D WST differ slightly on classification of bricks and soil and asphalt and bitumen. On Indian Pines in general 3D FST corrects the edges that 3D WST makes mistakes on. 3D WST also mistakes a large portion of soybean notill for corn notill that 3D FST corrects. There is spatial smoothing present in both 3D WST and 3D FST.

On the other hand, because of sparse and compact structure of the ground truth it is difficult to gain valuable geometric insight on the per class accuracies of Botswana and Smith island. For Smith Island, both 3D FST and 3D WST give reasonable seeming estimates with shapes from the false color image being recognizable in the classification maps. For Botswana the structure of the ground truth besides the water is especially hard to tell from the false color image, and both 3D FST and 3D WST give abstract results that look appealing but have a different amount of smoothness.

This spatial smoothing is largely influenced by the choices of M , M' , M'' . The choice of these frequency/support parameters is what determines the size of the spatial neighborhood from which spectral-spatial features will be extracted for a single pixel. For example, for PaviaU the window input into the scattering network was 19, since each level of filters were size 7. This is not dissimilar to other 3D methods in the

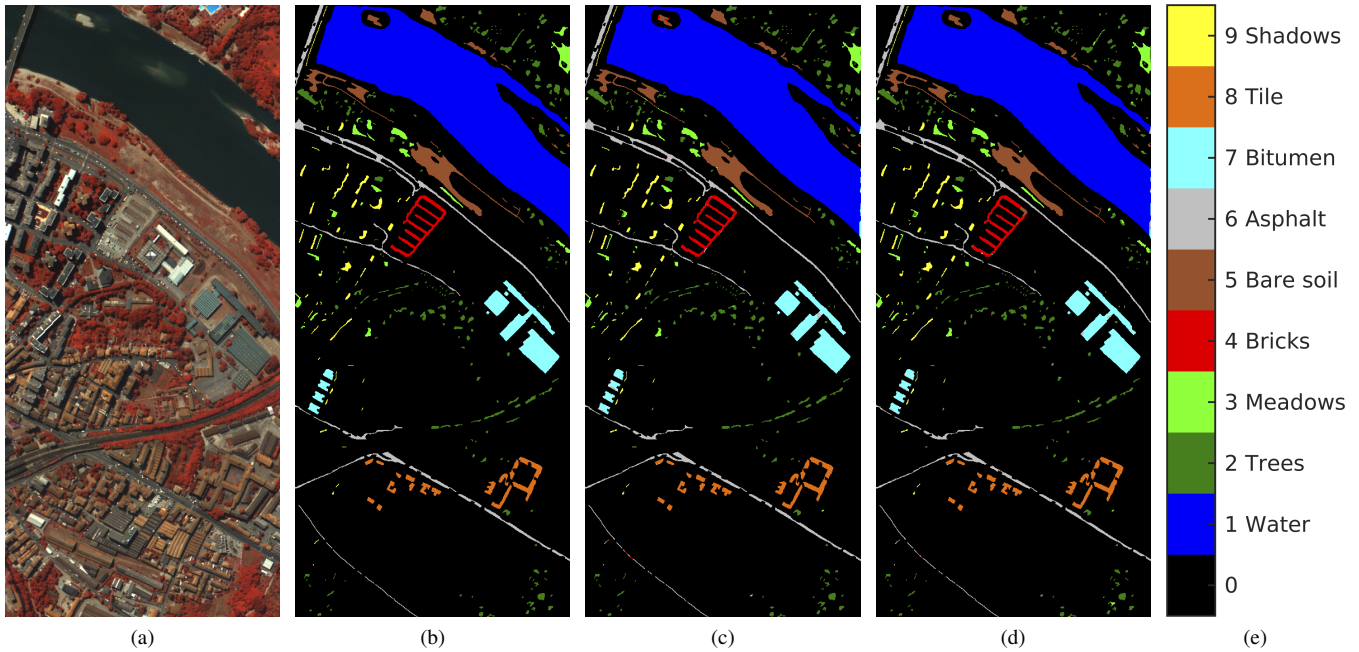


Fig. 4. Pavia Center (a) False color image and (b) Ground Truth Labels. Classification results for (c) 3D WST and (d) 3D FST. (e) Class Labels.

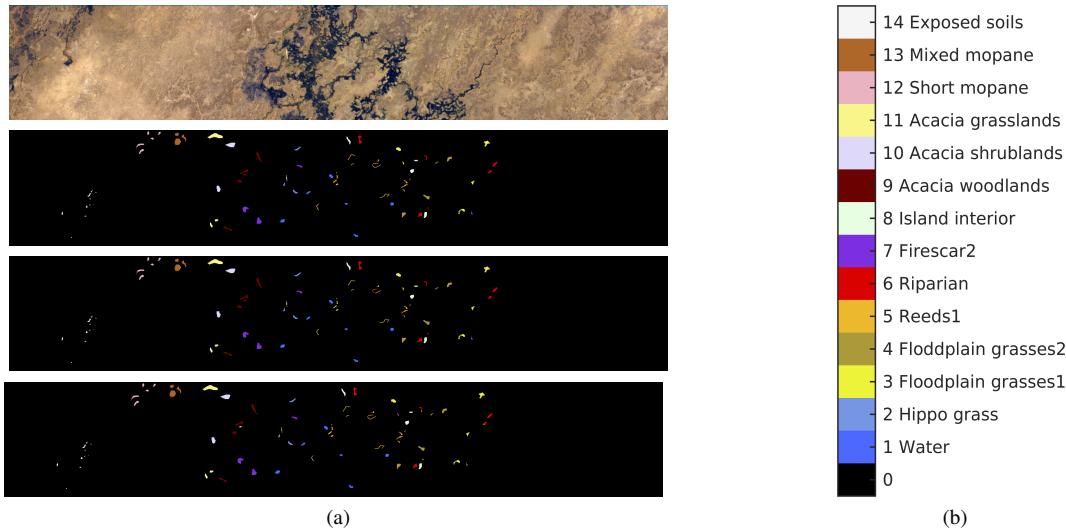


Fig. 5. From top to bottom in (a): Botswana False color image, Ground Truth Labels, classification results for 3D WST, and for 3D FST. Class labels in (b).

literature. The choice is the same in 3D WST [17], and 3D CNNs used input windows of spatial size 13 [22], 27 and 29 [5].

In Indian Pines the median number of samples per class when 10% of data is used for training is 47. In this dearth of training data, 3D methods that require no training for feature extraction by far outperform multiple 3D CNN methods which require much more training data to reach the same OA [5], [22]. However as seen in Table VIII there are still some trainable methods that are very competitive at 10% training data, though they are less competitive at 5% [7], [8]. The 3D methods in the table outperformed less spectral-spatial methods [4], [13], [21], [29]. Overall, the most powerful methods are the two time-frequency methods. Our method and

He *et al.*'s method [11] are within a margin of error of each other. Though [11] reports that 3D DLRGF+LS is their best method, they also include a classification performance for 3D DLRGF+SVM of 96.29 (± 0.96) which is higher than that for 3D DLRGF+LS but still within a margin or error of our result. When an SVM is used for classification 3D FST begins to outperform He *et al.*'s 3D DLRGF method at low training set sizes: At 1% training data 3D FST has 80.44 (± 1.63) OA while 3D DLRGF+SVM has 77.96 (± 0.81). However using a more powerful LS-based collaborative classifier He *et al.* was able to achieve a more competitive OA of 83.59 (± 0.81) (this edge is not as apparent at larger training set sizes as seen in Table VIII). We leave the pairing of our feature extraction method with more sophisticated classification techniques to

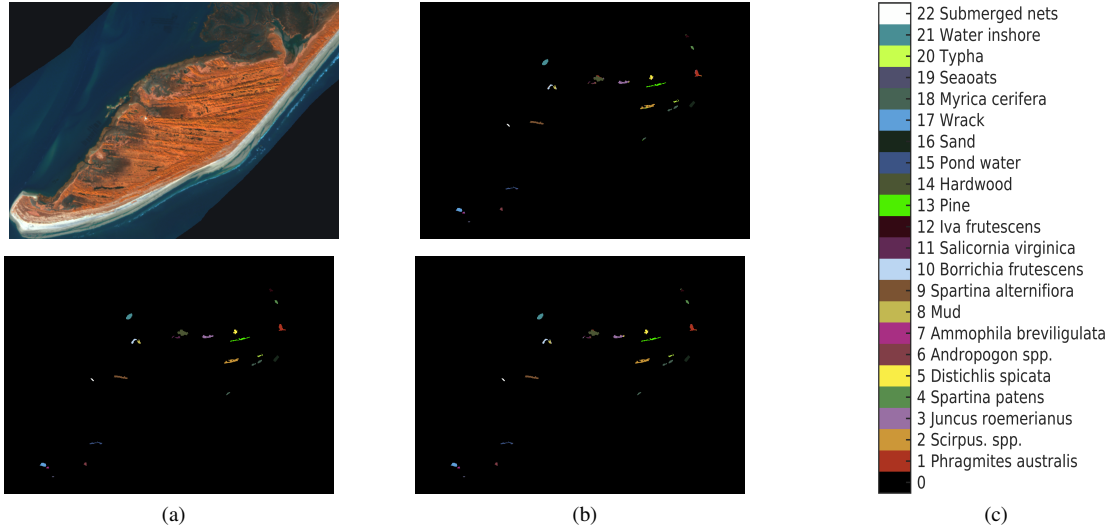


Fig. 6. Smith Island (a) False color image (top) and Ground Truth Labels (bottom). Classification results (b) for 3D WST (top) and 3D FST (bottom). Class labels in (c).

TABLE III

CLASSIFICATION ACCURACY FOR INDIAN PINES ACROSS 10 TRIALS ON 10% OF THE DATA (THE TRAINING SET FROM [7]) WITH A LINEAR SVM.

Class	Train	Test	3D WST	3D FST
1	5	41	83.90 (± 20.05)	94.39 (± 10.54)
2	143	1285	96.30 (± 1.73)	98.42 (± 0.83)
3	83	747	95.31 (± 2.08)	98.61 (± 0.89)
4	23	214	94.02 (± 3.40)	98.41 (± 2.37)
5	50	433	95.52 (± 3.01)	96.88 (± 2.89)
6	75	655	98.75 (± 0.61)	98.79 (± 0.66)
7	3	25	94.00 (± 6.04)	95.60 (± 5.80)
8	49	429	98.41 (± 1.25)	99.91 (± 0.16)
9	2	18	77.78 (± 21.44)	87.78 (± 12.78)
10	97	875	92.27 (± 2.14)	96.70 (± 1.73)
11	247	2208	96.11 (± 1.08)	98.90 (± 0.75)
12	61	532	93.53 (± 2.55)	97.29 (± 1.09)
13	21	184	98.70 (± 1.78)	97.77 (± 2.68)
14	129	1136	98.35 (± 0.54)	99.52 (± 0.53)
15	38	348	94.97 (± 2.51)	97.76 (± 1.64)
16	10	83	96.99 (± 2.80)	95.54 (± 3.55)
OA			95.98 (± 0.46)	98.37 (± 0.28)
AA			94.06 (± 2.01)	97.02 (± 1.24)
K			95.41 (± 0.52)	98.14 (± 0.32)

TABLE IV

CLASSIFICATION ACCURACY FOR PAVIAU ACROSS 10 TRIALS ON 10% OF THE DATA (THE TRAINING SET FROM [17]) WITH A LINEAR SVM.

Class	Train	Test	3D WST	3D FST
1	658	5973	99.31 (± 0.26)	99.52 (± 0.24)
2	1828	16821	99.83 (± 0.13)	99.87 (± 0.10)
3	208	1891	96.49 (± 0.96)	99.13 (± 0.77)
4	305	2759	98.50 (± 0.53)	98.63 (± 0.59)
5	135	1210	99.65 (± 0.46)	99.68 (± 0.39)
6	503	4526	99.92 (± 0.12)	99.98 (± 0.06)
7	133	1197	98.44 (± 0.66)	99.54 (± 0.35)
8	368	3314	97.76 (± 0.68)	99.30 (± 0.34)
9	95	852	97.58 (± 1.76)	98.80 (± 1.01)
OA			99.22 (± 0.10)	99.61 (± 0.09)
AA			98.61 (± 0.24)	99.38 (± 0.17)
K			98.97 (± 0.14)	99.49 (± 0.12)

TABLE V

CLASSIFICATION ACCURACY FOR PAVIA CENTRE ACROSS 10 TRIALS ON 1% OF THE DATA WITH A LINEAR SVM.

Class	Train	Test	3D WST	3D FST
1	652	64626	99.84 (± 0.08)	99.83 (± 0.07)
2	65	6443	96.73 (± 1.46)	97.42 (± 1.09)
3	29	2876	92.90 (± 1.74)	93.32 (± 1.71)
4	21	2119	96.06 (± 2.74)	95.34 (± 3.16)
5	65	6484	98.06 (± 0.91)	98.54 (± 1.21)
6	75	7510	98.01 (± 1.10)	98.42 (± 0.72)
7	72	7215	96.92 (± 1.34)	95.93 (± 1.28)
8	31	3091	99.66 (± 0.30)	99.37 (± 0.78)
9	21	2144	94.32 (± 2.24)	97.08 (± 1.30)
OA			98.80 (± 0.12)	98.87 (± 0.17)
AA			96.95 (± 0.43)	97.25 (± 0.51)
K			97.94 (± 0.21)	98.07 (± 0.30)

future work.

On PaviaU the median number of samples per class when 10% of data is used for training is 305, leading to a slightly more favorable situation than in Indian Pines for a trainable feature extractor. In Table IX we see a 3D CNN network performs just slightly below 3D FST, but is our closest competitor at 10% training data. At 200 samples 3D FST is by far SoA. 3D FST outperforms all 3D wavelet methods on PaviaU, the methods that stand out as our greatest competitors for PaviaU are all neural network based methods. Some results in the literature are also reported at a variety of training set

TABLE VI
CLASSIFICATION ACCURACY FOR BOTSWANA ACROSS 10 TRIALS ON 5% OF THE DATA (THE TRAINING SET FROM [17]) WITH A LINEAR SVM.

Class	Train	Test	3D WST	3D FST
1	14	256	99.96 (± 0.12)	99.06 (± 1.21)
2	6	95	98.11 (± 5.63)	96.42 (± 6.16)
3	13	238	97.27 (± 1.92)	95.97 (± 2.99)
4	11	204	99.61 (± 0.83)	99.95 (± 0.16)
5	14	255	86.94 (± 7.82)	88.67 (± 8.86)
6	14	255	93.69 (± 8.05)	97.65 (± 2.98)
7	13	246	99.80 (± 0.44)	100.00 (± 0.00)
8	11	192	99.43 (± 1.46)	99.43 (± 1.81)
9	16	298	97.55 (± 2.21)	98.89 (± 1.81)
10	13	235	99.32 (± 0.73)	100.00 (± 0.00)
11	16	289	97.58 (± 1.85)	97.85 (± 4.92)
12	10	171	98.13 (± 1.98)	97.60 (± 3.17)
13	14	254	99.33 (± 1.64)	99.92 (± 0.25)
14	5	90	86.78 (± 7.83)	88.78 (± 9.24)
OA			96.98 (± 1.06)	97.55 (± 0.92)
AA			96.68 (± 1.06)	97.16 (± 1.05)
K			96.73 (± 1.15)	97.35 (± 1.00)

TABLE VII
CLASSIFICATION ACCURACY FOR SMITH ISLAND ACROSS 10 TRIALS ON 5% OF THE DATA WITH A LINEAR SVM.

Class	Train	Test	3D WST	3D FST
1	9	187	90.64 (± 3.99)	97.33 (± 1.75)
2	12	234	89.44 (± 8.03)	96.45 (± 4.16)
3	9	175	90.91 (± 4.84)	94.86 (± 5.28)
4	3	63	91.27 (± 9.62)	96.03 (± 7.96)
5	4	93	91.51 (± 3.94)	92.37 (± 4.13)
6	2	55	85.09 (± 13.73)	90.00 (± 9.97)
7	1	31	67.10 (± 29.67)	91.94 (± 18.95)
8	3	67	93.28 (± 5.23)	93.28 (± 8.33)
9	10	190	97.95 (± 2.55)	97.68 (± 2.84)
10	4	86	87.56 (± 14.71)	90.58 (± 12.74)
11	3	73	67.95 (± 14.51)	79.04 (± 10.69)
12	2	56	79.11 (± 19.20)	94.64 (± 6.24)
13	8	158	99.75 (± 0.44)	100.00 (± 0.00)
14	16	312	92.44 (± 4.00)	97.66 (± 2.42)
15	5	100	90.80 (± 5.96)	95.10 (± 4.25)
16	7	152	100.00 (± 0.00)	100.00 (± 0.00)
17	7	137	96.42 (± 4.64)	97.59 (± 2.46)
18	8	159	95.60 (± 2.58)	98.99 (± 1.97)
19	1	17	98.24 (± 3.97)	100.00 (± 0.00)
20	2	42	77.38 (± 15.40)	87.86 (± 12.82)
21	10	196	100.00 (± 0.00)	100.00 (± 0.00)
22	1	33	100.00 (± 0.00)	100.00 (± 0.00)
OA			92.39 (± 1.19)	96.28 (± 0.84)
AA			90.11 (± 1.84)	95.06 (± 1.30)
K			91.88 (± 1.27)	96.02 (± 0.89)

sizes. 3D FST outperforms 3D DTW [12] at 5% of training data (98.6 vs 99.06 (± 0.12)) and 2D CNN at 6% of data (98.35 vs 99.20 (± 0.11)). There are competitive results such as the 2D capsule network by Deng *et al.* [6] at 60 samples

TABLE VIII
METHOD COMPARISON FOR INDIAN PINES AT 5% AND 10% FOR TRAINING DATA.

Method	5%	10%
3D FST	96.17 (± 0.96)	98.37 (± 0.28)
3D DLRGF+SVM [11]	96.29 (± 0.96)	-
3D DLRGF+LS [11]	96.16 (± 0.96)	-
3D WST+RBF-SVM [17]	-	94.46
3D WST	91.60 (± 0.91)	95.98 (± 0.46)
3D DWT-FB [16]	-	95.43
3D DWT [12]	94.5	-
3D WT+SRC [15]	96.04	-
NN/CNN [7]	94.9	98.23
2D CNN [8]	90.01	97.45
1D LSTM [20]	-	90.93

TABLE IX
METHOD COMPARISON FOR PAVIA U AT 10% OF TRAINING DATA AND 200 SAMPLES PER CLASS FOR TRAINING DATA.

Method	200 samp	10%
3D FST	98.55 (± 0.21)	99.61 (± 0.09)
3D CNN [5]	-	99.54
3D RCNN [22]	-	62
3D WST+RBF-SVM [17]	-	99.3
3D WST	98.16 (± 0.11)	99.22 (± 0.10)
3D DWT-FB [16]	-	95.45
2D CNN [8]	95.97	-
1D DBN [23]	93.11	-
1D CNN [21]	92.56	-

per class which performs within a margin of error of 3D FST (95.9 (± 1.38) vs 95.35 (± 0.53)). At 9% of training data Ma *et al.*'s NN+CNN method [7] performs well though they only report 1 trial (99.86 vs 99.55 (± 0.07)). And at 3 samples, 3D WT [14] performs within a margin or error of our method also (64.32 vs 64.09 (± 5.71)). Overall, across all training set sizes, 3D FST performs at the SoA level on PaviaU.

The other datasets are less ubiquitous in the literature so we briefly summarize their performance versus the literature here. For Botswana 3D FST with a linear SVM greatly outperforms CNN methods [22], [26], and a 3D wavelet method [16]. On PaviaC, using less training data 3D FST outperforms a 3D CNN method [22], and at 1% training data and 30 samples per class our method beats spatial regularized spectral CNN method [4] and a manifold learning approach [46].

V. CONCLUSION

In this paper we have proposed a three-dimensional Fourier scattering transform for HSI classification. This method has the neural network like benefits of heirarchical feature extraction while bypassing the training process which is computationally expensive in both the amount of required training data and training time. Our three dimensional time-frequency features are well suited for HSI data since they decompose the HSI into multi-frequency bands and remove small perturbations such as noise. The 3D FST is particularly effective when

there is limited training data. As supported by the experimental results, 3D FST achieved SoA performance on four benchmark datasets, all while executing within a few minutes on a conventional GPU, and using a typical SVM for classification. An advantage of our method is its compatibility with conventional deep learning implementations. This readily allows for a shift from the pre-processing based classification with a linear SVM we presented to an end-to-end feature extraction and classification deep network. Our future work investigates this hybridization of scattering transforms with deep learning where the classification is performed with a neural network following a tunable scattering transform that serves as a feature extractor, and both are trained jointly. This has the potential to improve classification performance further as both the classification and feature filters will be learned for each the dataset.

ACKNOWLEDGMENT

Ilya Kavalero and Rama Chellappa acknowledge the support of the MURI from the Army Research Office under the Grant No. W911NF-17-1-0304. This is part of the collaboration between US DOD, UK MOD and UK Engineering and Physical Research Council (EPSRC) under the Multidisciplinary University Research Initiative. Weilin Li was supported by the Ann G. Wylie Dissertation Fellowship during the Spring 2018 semester at the University of Maryland and by the James C. Alexander Prize for Graduate Research. Wojciech Czaja is supported in part by LTS through Maryland Procurement Office and the NSF DMS 1738003 grant.

REFERENCES

- [1] A. F. H. Goetz, "Three decades of hyperspectral remote sensing of the Earth: A personal view," *Remote Sensing of Environment*, vol. 113, pp. S5–S16, Sep. 2009. [Online]. Available: <http://www.sciencedirect.com/science/article/pii/S003442570900073X>
- [2] N. Skytland, "What is NASA doing with Big Data today?" *open.NASA.gov*, 2012. [Online]. Available: <https://open.nasa.gov/blog/what-is-nasa-doing-with-big-data-today/>
- [3] L. He, J. Li, C. Liu, and S. Li, "Recent advances on spectralspatial hyperspectral image classification: An overview and new guidelines," *IEEE Transactions on Geoscience and Remote Sensing*, vol. 56, no. 3, pp. 1579–1597, March 2018.
- [4] J. Acquarelli, E. Marchiori, L. M. C. Buydens, T. Tran, and T. van Laarhoven, "Spectral-Spatial Classification of Hyperspectral Images: Three Tricks and a New Learning Setting," *Remote Sensing*, vol. 10, no. 7, p. 1156, Jul. 2018. [Online]. Available: <https://www.mdpi.com/2072-4292/10/7/1156>
- [5] Y. Chen, H. Jiang, C. Li, X. Jia, and P. Ghamisi, "Deep Feature Extraction and Classification of Hyperspectral Images Based on Convolutional Neural Networks," *IEEE Transactions on Geoscience and Remote Sensing*, vol. 54, no. 10, pp. 6232–6251, Oct. 2016.
- [6] F. Deng, S. Pu, X. Chen, Y. Shi, T. Yuan, and S. Pu, "Hyperspectral Image Classification with Capsule Network Using Limited Training Samples," *Sensors (Basel, Switzerland)*, vol. 18, no. 9, Sep. 2018. [Online]. Available: <https://www.ncbi.nlm.nih.gov/pmc/articles/PMC6165568/>
- [7] X. Ma, J. Geng, and H. Wang, "Hyperspectral image classification via contextual deep learning," *EURASIP Journal on Image and Video Processing*, vol. 2015, no. 1, p. 20, Jul. 2015. [Online]. Available: <https://doi.org/10.1186/s13640-015-0071-8>
- [8] H. Liang and Q. Li, "Hyperspectral Imagery Classification Using Sparse Representations of Convolutional Neural Network Features," *Remote Sensing*, vol. 8, no. 2, p. 99, Jan. 2016. [Online]. Available: <https://www.mdpi.com/2072-4292/8/2/99>
- [9] T. C. Bau, S. Sarkar, and G. Healy, "Hyperspectral region classification using a three-dimensional gabor filterbank," *IEEE Transactions on Geoscience and Remote Sensing*, vol. 48, no. 9, pp. 3457–3464, 2010.
- [10] S. Jia, L. Shen, and Q. Li, "Gabor Feature-Based Collaborative Representation for Hyperspectral Imagery Classification," *IEEE Transactions on Geoscience and Remote Sensing*, vol. 53, no. 2, pp. 1118–1129, Feb. 2015.
- [11] L. He, J. Li, A. Plaza, and Y. Li, "Discriminative Low-Rank Gabor Filtering for SpectralSpatial Hyperspectral Image Classification," *IEEE Transactions on Geoscience and Remote Sensing*, vol. 55, no. 3, pp. 1381–1395, Mar. 2017.
- [12] X. Cao, L. Xu, D. Meng, Q. Zhao, and Z. Xu, "Integration of 3-dimensional discrete wavelet transform and Markov random field for hyperspectral image classification," *Neurocomputing*, vol. 226, pp. 90–100, Feb. 2017. [Online]. Available: <http://www.sciencedirect.com/science/article/pii/S0925231216314357>
- [13] G. Franchi and J. Angulo, "A deep spatial/spectral descriptor of hyperspectral texture using scattering transform," in *2016 IEEE International Conference on Image Processing (ICIP)*, Sep. 2016, pp. 3568–3572.
- [14] S. Jia, J. Hu, Y. Xie, L. Shen, X. Jia, and Q. Li, "Gabor Cube Selection Based Multitask Joint Sparse Representation for Hyperspectral Image Classification," *IEEE Transactions on Geoscience and Remote Sensing*, vol. 54, no. 6, pp. 3174–3187, Jun. 2016.
- [15] L. Shen and S. Jia, "Three-Dimensional Gabor Wavelets for Pixel-Based Hyperspectral Imagery Classification," *IEEE Transactions on Geoscience and Remote Sensing*, vol. 49, no. 12, pp. 5039–5046, Dec. 2011.
- [16] Y. Qian, M. Ye, and J. Zhou, "Hyperspectral Image Classification Based on Structured Sparse Logistic Regression and Three-Dimensional Wavelet Texture Features," *IEEE Transactions on Geoscience and Remote Sensing*, vol. 51, no. 4, pp. 2276–2291, Apr. 2013.
- [17] Y. Y. Tang, Y. Lu, and H. Yuan, "Hyperspectral image classification based on three-dimensional scattering wavelet transform," *IEEE Transactions on Geoscience and Remote Sensing*, vol. 53, no. 5, pp. 2467–2480, 2015.
- [18] W. Czaja and W. Li, "Analysis of time-frequency scattering transforms," *Applied and Computational Harmonic Analysis*, 2017.
- [19] —, "Rotationally invariant time-frequency scattering transforms," *arXiv preprint arXiv:1710.06889*, 2017.
- [20] Y. Guo, S. Han, H. Cao, Y. Zhang, and Q. Wang, "Guided filter based Deep Recurrent Neural Networks for Hyperspectral Image Classification," *Procedia Computer Science*, vol. 129, pp. 219–223, Jan. 2018. [Online]. Available: <http://www.sciencedirect.com/science/article/pii/S1877050918302710>
- [21] W. Hu, Y. Huang, L. Wei, F. Zhang, and H. Li, "Deep Convolutional Neural Networks for Hyperspectral Image Classification," 2015. [Online]. Available: <https://www.hindawi.com/journals/js/2015/258619/>
- [22] X. Yang, Y. Ye, X. Li, R. Y. K. Lau, X. Zhang, and X. Huang, "Hyperspectral Image Classification With Deep Learning Models," *IEEE Transactions on Geoscience and Remote Sensing*, vol. 56, no. 9, pp. 5408–5423, Sep. 2018.
- [23] P. Zhong, Z. Gong, S. Li, and C. Schnlieb, "Learning to Diversify Deep Belief Networks for Hyperspectral Image Classification," *IEEE Transactions on Geoscience and Remote Sensing*, vol. 55, no. 6, pp. 3516–3530, Jun. 2017.
- [24] S. Mallat, "Group invariant scattering," *Communications on Pure and Applied Mathematics*, vol. 65, no. 10, pp. 1331–1398, 2012.
- [25] P.-H. Hsu, "Evaluating the Initialization Methods of Wavelet Networks for Hyperspectral Image Classification," *ISPRS - International Archives of the Photogrammetry, Remote Sensing and Spatial Information Sciences*, vol. 41B7, pp. 83–89, Jun. 2016. [Online]. Available: <http://adsabs.harvard.edu/abs/2016ISPAr41B7..83H>
- [26] H. Gao, S. Lin, Y. Yang, C. Li, and M. Yang, "Convolution Neural Network Based on Two-Dimensional Spectrum for Hyperspectral Image Classification," 2018. [Online]. Available: <https://www.hindawi.com/journals/js/2018/8602103/>
- [27] W. Czaja, W. Li, and I. Kavalero, "Scattering transforms and classification of hyperspectral images," in *Algorithms and Technologies for Multispectral, Hyperspectral, and Ultraspectral Imagery XXIV*, D. W. Messinger and M. Velez-Reyes, Eds. Orlando, United States: SPIE, May 2018, p. 17. [Online]. Available: <https://www.spiedigitallibrary.org/conference-proceedings-of-spie/10644/2305152/Scattering-transforms-and-classification-of-hyperspectral-images/10.1117/12.2305152.full>
- [28] P.-H. Hsu, "Classification of hyperspectral images using wavelet networks," vol. 1, pp. 535–544, Jan. 2006.

- [29] H. Lee and H. Kwon, "Going Deeper with Contextual CNN for Hyperspectral Image Classification," *IEEE Transactions on Image Processing*, vol. 26, no. 10, pp. 4843–4855, Oct. 2017. [Online]. Available: <http://arxiv.org/abs/1604.03519>
- [30] A. Mughees, A. Ali, and L. Tao, "Hyperspectral image classification via shape-adaptive deep learning," in *2017 IEEE International Conference on Image Processing (ICIP)*, Sep. 2017, pp. 375–379.
- [31] P. S. Ashitha, V. Sowmya, and K. P. Soman, "Classification of hyperspectral images using scattering transform," *International Journal of Scientific & Engineering Research*, vol. 5, no. 7, p. 5, 2014.
- [32] S. Sabour, N. Frosst, and G. E. Hinton, "Dynamic Routing Between Capsules," *arXiv:1710.09829 [cs]*, Oct. 2017, arXiv: 1710.09829. [Online]. Available: <http://arxiv.org/abs/1710.09829>
- [33] N. Haridas, V. Sowmya, and K. P. Soman, "Comparative Analysis of Scattering and Random Features in Hyperspectral Image Classification," *Procedia Computer Science*, vol. 58, pp. 307–314, Jan. 2015. [Online]. Available: <http://www.sciencedirect.com/science/article/pii/S1877050915021365>
- [34] L. He, Y. Li, X. Li, and W. Wu, "Spectralspatial classification of hyperspectral images via spatial translation-invariant wavelet-based sparse representation," *IEEE Transactions on Geoscience and Remote Sensing*, vol. 53, no. 5, pp. 2696–2712, 2015.
- [35] J. Bruna and S. Mallat, "Invariant scattering convolution networks," *IEEE Transactions on Pattern Analysis and Machine Intelligence*, vol. 35, no. 8, pp. 1872–1886, 2013.
- [36] C. L. Bennett, M. R. Carter, D. J. Fields, and F. D. Lee, "Infrared hyperspectral imaging results from vapor plume experiments," *Proc. SPIE*, vol. 2480, no. 19, pp. 435–444, 1995.
- [37] E. N. Lewis, P. J. Treado, R. C. Reeder, G. M. Story, A. E. Dowrey, C. Marcott, and I. W. Levin, "Fourier transform spectroscopic imaging using an infrared focal-plane array detector," *Analytical Chemistry*, vol. 67, no. 19, pp. 3377–3381, 1995.
- [38] K. Gröchenig, *Foundations of time-frequency analysis*. Springer Science & Business Media, 2013.
- [39] J. Andén and S. Mallat, "Deep scattering spectrum," *IEEE Transactions on Signal Processing*, vol. 62, no. 16, pp. 4114–4128, 2014.
- [40] M. F. Baumgardner, L. L. Biehl, and D. A. Landgrebe, "220 band aviris hyperspectral image data set: June 12, 1992 indian pine test site 3," Sep 2015. [Online]. Available: <https://purr.purdue.edu/publications/1947/1>
- [41] F. D. Acqua, P. Gamba, and A. Ferrari, "Exploiting spectral and spatial information for classifying hyperspectral data in urban areas," in *IGARSS 2003. 2003 IEEE International Geoscience and Remote Sensing Symposium. Proceedings (IEEE Cat. No.03CH37477)*, vol. 1, July 2003, pp. 464–466 vol.1.
- [42] A. L. Neuenschwander, M. M. Crawford, and S. Ringrose, "Monitoring of seasonal flooding in the okavango delta using eo-1 data," in *IEEE International Geoscience and Remote Sensing Symposium*, vol. 6, 2002, pp. 3124–3126 vol.6.
- [43] P. Gamba, "A collection of data for urban area characterization," in *Geoscience and Remote Sensing Symposium, 2004. IGARSS'04. Proceedings. 2004 IEEE International*, vol. 1. IEEE, 2004.
- [44] C. M. Bachmann, T. F. Donato, G. M. Lamela, W. J. Rhea, M. H. Bettenhausen, R. A. Fusina, K. R. D. Bois, J. H. Porter, and B. R. Truitt, "Automatic classification of land cover on Smith Island, VA, using HyMAP imagery," *IEEE Transactions on Geoscience and Remote Sensing*, vol. 40, no. 10, pp. 2313–2330, Oct. 2002.
- [45] "Hyperspectral remote sensing scenes," http://www.ehu.eus/ccwintco/index.php/Hyperspectral_Remote_Sensing_Scenes, accessed: 01-01-2018.
- [46] L. Zhang, Q. Zhang, B. Du, X. Huang, Y. Y. Tang, and D. Tao, "Simultaneous Spectral-Spatial Feature Selection and Extraction for Hyperspectral Images," *IEEE Transactions on Cybernetics*, vol. 48, no. 1, pp. 16–28, Sep. 2016.



Ilya Kavalero received the B.Sc. degree in Chemistry at the George Washington University in Washington D.C. in 2013. He is currently pursuing the Ph.D. degree in Electrical Engineering at the University of Maryland, College Park.

He was a research intern at Google Cambridge in 2018, and Google Mountain View in 2019. His research interests include scattering transforms, deep learning, generative adversarial networks, and computer vision.

Weilin Li received the Ph.D. degree in Mathematics at the Norbert Wiener Center, University of Maryland, College Park in the spring of 2018. He is currently a Courant Instructor at the Courant Institute of Mathematical Sciences, New York University.

His research interests include scattering transforms, spectral super-resolution, and Harmonic analysis on graphs and fractals.

Wojciech Czaja received the Ph.D. degree in Mathematics from Washington University in St. Louis. He is currently a Professor of Mathematics at University of Maryland College Park, a member of the Norbert Wiener Center, of the Center for Scientific Computation and Mathematical Modeling, and a Marie Curie Fellow.



Rama Chellappa (F92) received the Ph.D. degree from Purdue University in 1981. He is a Distinguished University Professor and a Minta Martin Professor of engineering with the Electrical and Computer Engineering Department, University of Maryland at College Park. His current research interests are face and gait analysis, 3-D modeling from video, image and video-based recognition and exploitation, compressive sensing, and hyper spectral processing. He has received numerous research, teaching, innovation, and service awards from UMD,

IEEE, IAPR, and IBM. He is a fellow of AAAI, AAAS, ACM, IAPR, and OSA.